



Article

Characterizing the Topographic Changes and Land Subsidence Associated with the Mountain Excavation and City Construction on the Chinese Loess Plateau

Chuanhao Pu ¹, Qiang Xu ^{1,*}, Kuanyao Zhao ¹, Yanan Jiang ¹, Lina Hao ¹, Jialiang Liu ¹, Wanlin Chen ¹ and Pinglang Kou ²

- ¹ State Key Laboratory of Geohazard Prevention and Geoenvironment Protection, Chengdu University of Technology, Chengdu 610059, China; puchuanhao@stu.cdut.edu.cn (C.P.); zhaokuanyao@stu.cdut.edu.cn (K.Z.); Jiangyanan@cdut.edu.cn (Y.J.); haolina13@cdut.edu.cn (L.H.); liujial3385@stu.cdut.edu.cn (J.L.); chenwanlin@stu.cdut.edu.cn (W.C.)
- ² The Chongqing Engineering Research Center for Spatial Big Data Intelligent Technology, Chongqing University of Posts and Telecommunications, Chongqing 400065, China; koupl@cqupt.edu.cn
- * Correspondence: xq@cdut.edu.cn



Citation: Pu, C.; Xu, Q.; Zhao, K.; Jiang, Y.; Hao, L.; Liu, J.; Chen, W.; Kou, P. Characterizing the Topographic Changes and Land Subsidence Associated with the Mountain Excavation and City Construction on the Chinese Loess Plateau. *Remote Sens.* **2021**, *13*, 1556. <https://doi.org/10.3390/rs13081556>

Academic Editor:
Francesca Ardizzone

Received: 23 March 2021
Accepted: 14 April 2021
Published: 16 April 2021

Publisher's Note: MDPI stays neutral with regard to jurisdictional claims in published maps and institutional affiliations.



Copyright: © 2021 by the authors. Licensee MDPI, Basel, Switzerland. This article is an open access article distributed under the terms and conditions of the Creative Commons Attribution (CC BY) license (<https://creativecommons.org/licenses/by/4.0/>).

Abstract: A mega project, Mountain Excavation and City Construction (MECC), was launched in the hilly and gully region of the Chinese Loess Plateau in 2012, in order to address the shortage of available land and create new flat land for urban construction. However, large-scale land creation and urban expansion significantly alters the local geological environment, leading to severe ground deformation. This study investigated the topographic changes, ground deformation, and their interactions due to the MECC project in the Yan'an New District (YND). First, new surface elevations were generated using ZiYuan-3 (ZY-3) stereo images acquired after the construction in order to map the local topographic changes and the fill thickness associated with the MECC project. Then, the interferometric synthetic aperture radar (InSAR) time series and 32 Sentinel-1A images were used to assess the spatial patterns of the ground deformation in the YND during the postconstruction period (2017–2018). By combining the InSAR-derived results and topographic change features, the relationship between the ground deformation and large-scale land creation was further analyzed. The results indicated that the MECC project in the YND has created over 22 km² of flat land, including 10.8 km² of filled area, with a maximum fill thickness of ~110 m. Significant uneven ground deformation was detected in the land-creation area, with a maximum subsidence rate of approximately 121 mm/year, which was consistent with the field survey. The strong correlation between the observed subsidence patterns and the land creation project suggested that this recorded uneven subsidence was primarily related to the spatial distribution of the filling works, along with the changes in the thickness and geotechnical properties of the filled loess; moreover, rapid urbanization, such as road construction, can accelerate the subsidence process. These findings can guide improvements in urban planning and the mitigation of geohazards in regions experiencing large-scale land construction.

Keywords: topographic change; land subsidence; mountain excavation and city construction; SBAS-InSAR; Loess Plateau

1. Introduction

The Loess Plateau, covering an area of approximately 440,000 km² in north-central China, is the most widely distributed, thickest loess area in the world [1]. With the rapid promotion of the 'western development strategy' and the 'Belt and Road' policy in China, several mega engineering projects have been underway on the Loess Plateau, such as the 'Mountain Excavation and City Construction' (MECC) [2], the 'Gully Control and Highland Protection' (GCHP) [3] and the 'Gully Land Consolidation' (GLC) [4]. The pace and intensity of these projects far exceed the geological bearing capacity and therefore

exert a great impact on the geological environment, leading to the occurrence of frequent geohazards. In particular, the large-scale implementation of the MECC project, such as in the Lanzhou New District and the Yan'an New District (YND), will create new flat land for urban expansion by removing hilltops to fill the valley (Figure 1), but this will also significantly change the local geological environment (including topographical changes), [2] and will thus cause new environmental hazards, such as the postconstruction settlement of loess fill foundations [5]. Widespread land subsidence may cause damage to construction and urban infrastructure, including pipelines and roads, and may even affect the sustainable development of cities. Hence, the analysis of the relationship between ground deformation and the large-scale MECC project can aid in further understanding the mechanism of subsidence, and can ultimately better guide urban planning and disaster prevention and mitigation.

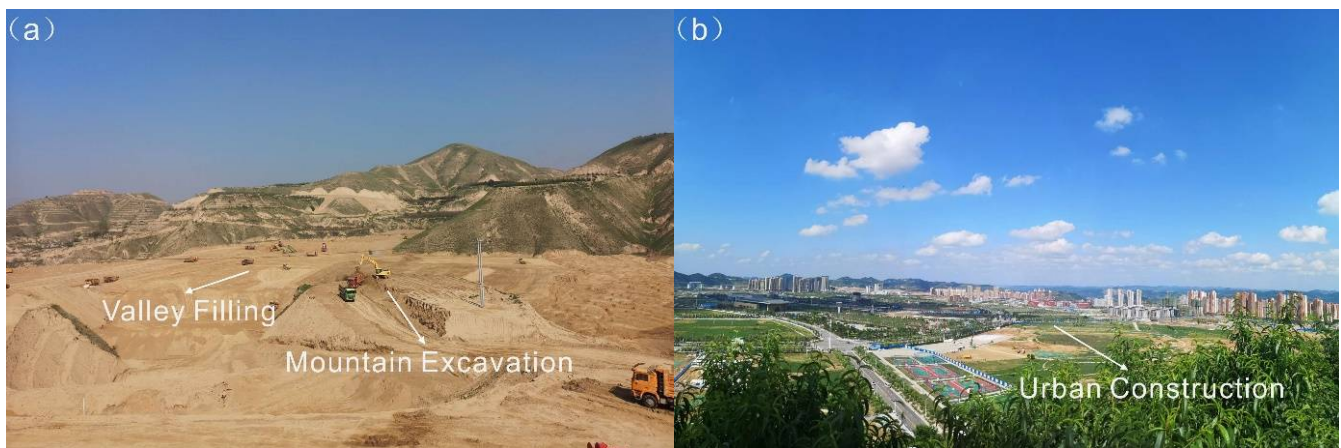


Figure 1. Mountain excavation and city construction in the YND. (a) Land creation in the loess hilly region; (b) Urban construction in the land-creation area.

Yan'an, Shaanxi Province, is a city with a severe shortage of available land, with approximately 500,000 people living within a Y-shaped urban area of only 36 km². In order to solve the problem of overcrowding in this historic city, the MECC project was started in April 2012 to create a new district of 78 km², known as the Yan'an New District [6]. The MECC project in the YND is regarded as the largest geotechnical project in a collapsible loess region worldwide [2]. This unprecedented large-scale land creation and rapid urbanization has drawn great attention from scientists and society. Although the large-scale construction of the MECC project can create more available space for urban expansion, it could also significantly alter the original topography and create large loess fill areas, which may cause severe land subsidence and pose new challenges for urban development [5,6]. Several studies have investigated the mechanism and spatiotemporal patterns of land subsidence in the YND using geodetic methods, such as leveling [7], global positioning systems (GPSs), and interferometric synthetic aperture radar (InSAR) [5]. The results of these previous studies have highlighted the driving effects of human activities associated with large-scale land creation on the development of ground subsidence in the YND. For example, the in situ monitoring of filled loess embankments has indicated that the subsidence of the fill body itself accounts for the majority of the total subsidence, and the filling work related to land creation is the primary cause of land subsidence in the YND [7]. Wu et al. (2019) assessed the spatiotemporal patterns of the subsidence in the YND based on the small baseline subset InSAR (SBAS-InSAR) technique, and confirmed the ability of the SBAS-InSAR method to detect surface deformation in the land creation region; the results indicated that the land subsidence is mainly caused by earth filling and building loads [5]. However, the spatial characteristics and interrelations of the local topographic changes and land subsidence associated with land creation are not yet fully understood, largely due to the absence of high accuracy postconstruction topographic

data that could reflect the surface processes caused by land creation and provide detailed information on the fill thickness.

Remote sensing technology has proven to be an effective tool for investigating land use and topographic changes, and for monitoring land subsidence [8–10]. Space-borne optical photogrammetry provides the capability to extract new surface elevation, and is widely used to estimate local topographic changes due to glacial activity, geological hazards, or human activities [11]. In recent years, with the rapid development of the InSAR technique, it has become feasible and reliable to map surface displacement at very high spatiotemporal resolutions in land-creation areas. Compared with ground-based geodetic methods, such as spirit leveling and GPS, the InSAR technique has the unique capability of monitoring large-scale surface deformation with high accuracy and high spatial resolution under all weather conditions [12,13], and it has been widely applied to the detection and monitoring of various geohazards, including earthquakes [14], landslides [15–17], land subsidence [18], and other geologic processes [8,19]. In particular, advanced multitemporal InSAR (MT-InSAR) methods, such as persistent scatterers InSAR (PS-InSAR) [20,21] and small baseline subset InSAR (SBAS-InSAR) [22], have been rapidly developed to reduce the effects of decorrelation and uneven atmospheric delay, and to remove the topographic phase, which are intrinsic limitations of the traditional differential InSAR (D-InSAR) method. Accordingly, MT-InSAR methods have facilitated the monitoring of ground deformation in many countries and cities, such as Mexico City [23,24], Italy [25,26], Hong Kong [12], Beijing [27,28], and Xi'an [29].

The main objectives of this study are (1) to characterize the spatiotemporal patterns of the topographic changes and land subsidence associated with the MECC project in the YND, and (2) to quantify the relationships between land subsidence and the MECC project in the YND. In this paper, we illustrate an integrated approach which uses space-borne optical photogrammetry, InSAR techniques and field surveys to investigate the topographic changes and ground deformation due to the large-scale MECC project and their interactions. First, space-borne optical photogrammetry was used to extract new surface elevations, and to map the local topographic and geomorphological changes caused by the MECC project. Moreover, the magnitude and spatial distribution of the ground deformation in the YND was derived from 32 Sentinel-1A images using the SBAS-InSAR method. Then, the relationships between the observed deformations and the large-scale MECC project were discussed in detail by combining the InSAR-derived results with the topographic change features and optical images. Finally, other possible natural and anthropogenic factors influencing ground settlement were analyzed and discussed. These results will facilitate a better understanding of the surface deformation induced by the MECC project, which can aid in urban planning and disaster prevention and mitigation in loess regions where large-scale land creation and rapid city construction projects occur.

2. Study Area

Yan'an city is located in the hilly-gully area of the south-central part of the Loess Plateau, China (Figure 2b). The old city is a typical linear city, with densely-distributed urban buildings along a Y-shaped river valley (Figure 2c). The narrow and long urban area of approximately 36 km² accommodates nearly 500,000 people, making the local construction land per capita far below the national standard for land utilization. Simultaneously, Yan'an city, as a revolutionary holy land of China, has over 140 historical relics [5]. However, in order to obtain more land for urban development, a large number of revolutionary sites have been occupied and destroyed, which intensified the competition between urban and landscape areas. With rapid urban development and population growth, the shortage of land resources for construction in the old city has further intensified, which has severely restricted the economic and social development of Yan'an city. In order to realize the sustainable development of urbanization, and to protect the historical and cultural heritage of revolutionary sacred land, the MECC project was implemented to create flat land and build the YND by removing the tops of loess mountains to fill in the valleys [2] (Figure 1).

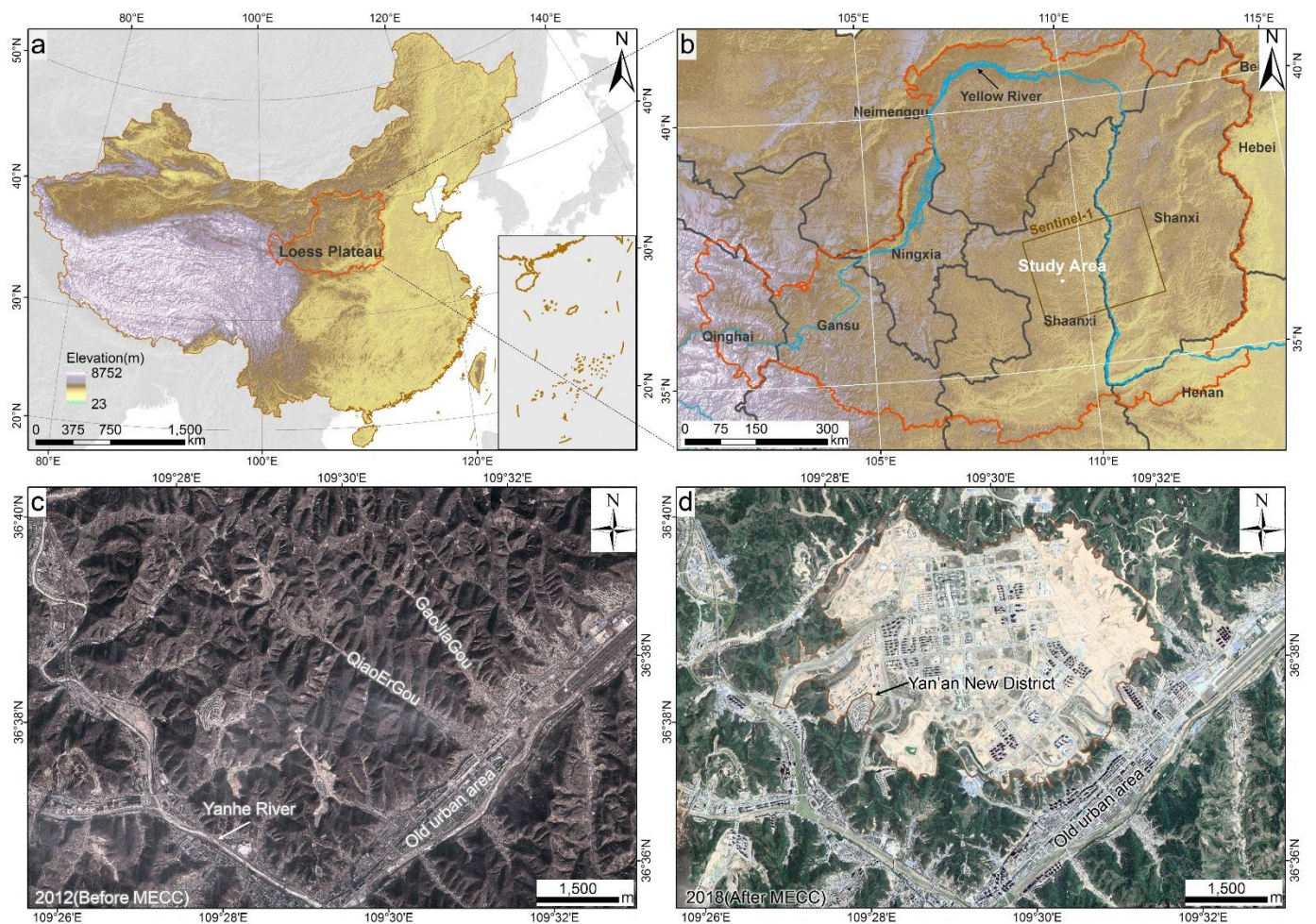


Figure 2. Administrative location of the study area. (a) Loess Plateau location; (b) study area location. The brown rectangle indicates the coverage of the selected Sentinel-1A images; (c,d) Google Earth images before and after the MECC project.

The earthwork project in the YND started on 17 April 2012, and was completed in August 2018, creating approximately 22.3 km² of flat land for urban construction (Figure 2d). The original topography of the YND was a typical loess hilly and gully landform with many gullies. The terrain elevation ranged from 950 to 1260 m, and the valley depths ranged from 100 to 150 m. Following the completion of the land creation project, the YND is now characterized by relatively flat topography (Figure 2d), with an average elevation of 1100 m. The study area is mainly covered by Middle Pleistocene Lishi loess and Late Pleistocene Malan loess with strong collapsibility, which have been the primary sources of material for the MECC project. The climate is characteristic of a semi-humid and semiarid continental monsoon climate, with an average annual temperature of 10.3 °C [4] and an average annual precipitation of approximately 562 mm. Nearly 70% of the annual precipitation is concentrated in the period from June to September [5].

3. Data and Methods

3.1. Datasets

3.1.1. ZY-3 Satellite Images

ZiYuan-3 (ZY-3) is the first Chinese civilian multispectral satellite with high-resolution optical stereoscopic mapping capability; it was launched on 9 January 2012 [30]. This satellite can compose three-line-array (TLA) stereo images from three panchromatic cameras at different viewing angles (forward, nadir and backward). A scene of ZY-3 TLA data consists of images viewed from the nadir, backward, and forward angles with spatial resolutions of

2.5 m, 3.5 m, and 3.5 m, respectively. The TLA stereo images of the ZY-3 satellite permit the generation of digital elevation models (DEMs) for the estimation of the terrain elevation and its changes [11]. The stereo-imagery pair composed of forward and backward view images are taken in almost identical lighting and weather conditions. Therefore, they are more applicable for DEM generation using automated DEM extraction techniques than the stereo pair taken by the cross-track orbits [31]. Moreover, rational polynomial coefficients (RPCs) are provided together with the ZY-3 TLA data, providing information on the mathematical transformation between the geographic coordinates and the image coordinates [32]. In this study, three image data sets with cloudless and clear features on 17 November 2013, 12 May 2015, and 13 October 2017 were collected from the Satellite Surveying and Mapping Application Center (SASMAC) and clipped to extract the DEM, in order to estimate the topographic change and fill thickness in the study area. Detailed information on ZY-3 is presented in Table 1.

Table 1. Detailed information on the datasets used in this study.

Data	Parameters	Description
ZY-3	Spatial resolution (m)	Nadir (2.5) Forward (3.5) Backward (3.5)
	Swath Width (km)	52
	Band	C
	Wavelength (cm)	5.6
Sentinel-1A	Orbit direction	Ascending
	Mean Incidence angle (°)	33.9
	Resolution (m) of Rg × Az	5 × 20
	Polarization	VV
	Number of images	32
	Date period	December 2017 to December 2018
Shuttle radar topography mission (SRTM)	Resolution (m)	30
Google Earth	Resolution (m)	0.48

3.1.2. SAR Data and Ancillary Data

The large-scale land creation projects and urban construction in the YND commenced in April 2012 and were still underway until August 2018, which induced great changes in the land surface. Therefore, in order to reduce the effect of the surface changes caused by land creation on the decorrelation of SAR images, and to acquire comprehensive and detailed surface deformation information on the entire YND, we collected 32 archived SAR images with a spatial resolution of 5 m × 20 m (range × azimuth) acquired from December 2018 to December 2019 by C-band Sentinel-1A satellites, with a sampling interval of 12 days. Moreover, precise orbit ephemerides (POEs) data from the European Space Agency were applied to the initial estimates of the interferometric baselines. In order to remove the topography-related phase from the interferometric phase and geocode the InSAR products, a shuttle radar topography mission (SRTM) with a spatial resolution of 30 m was applied as external DEM data in this study. Moreover, in order to explore the spatial association between the surface deformation and anthropogenic factors, multitemporal Google Earth images with a resolution of 0.48 m were utilized to aid in the interpretation and analysis of the results in this study. Detailed information about the SAR data used in this study is shown in Table 1, and their coverages are shown in Figure 2b.

3.2. Methods

3.2.1. Topographic Change Calculation

DEM extraction using stereo image pairs has developed into a relatively mature technology, which started from analytical stereo plotters in the 1980s [31]. With the development of digital image processing techniques, many commercial and open-source software programs have provided modules for DEM generation. In this study, the backward-forward image pairs provided by the ZY-3 TLA data were processed using the rational functional model (RFM) in TitanImage software in order to perform the extraction of the DEM (hereinafter ZY-3 DEM). The RFM is the major imaging geometric model currently employed for the block adjustment of most satellite images [33]. The RFM establishes a mathematical transformation between image coordinates and their corresponding object coordinates using RPCs [32]. However, DEM generation using RFM based solely on RPCs is biased, and needs ground control points (GCPs) to refine it, but we relied only on intensive and well-distributed tie points to enhance the solution because GCPs were unavailable [34]. Previous studies have documented that the DEM generated by ZY-3 stereo images can achieve high vertical accuracy with or without GCPs [30,31]. Hence, ZY-3 image data can be used to extract the DEM. In total, 61 evenly-distributed tie points were selected, and the ZY-3 DEM was generated with a spatial resolution of 5 m and the same projection information as the SRTM DEM.

Moreover, after we acquired the postconstruction ZY-3 DEM, the topographic changes in 2000–2013, 2000–2015 and 2000–2017 were estimated by calculating the difference between the SRTM and the ZY-3 DEMs (Figure 3). The DEMs were matched and resampled to the same resolution prior to the calculation, as relative geolocation errors are common between DEMs [8,11]. The elevation change results in 2000–2017 were employed in order to discuss the uncertainty excluding the YND affected by the MECC project. The mean and standard deviation of the elevation difference in non-YND areas were used to characterize the relative elevation accuracy of the ZY-3 DEM [11].

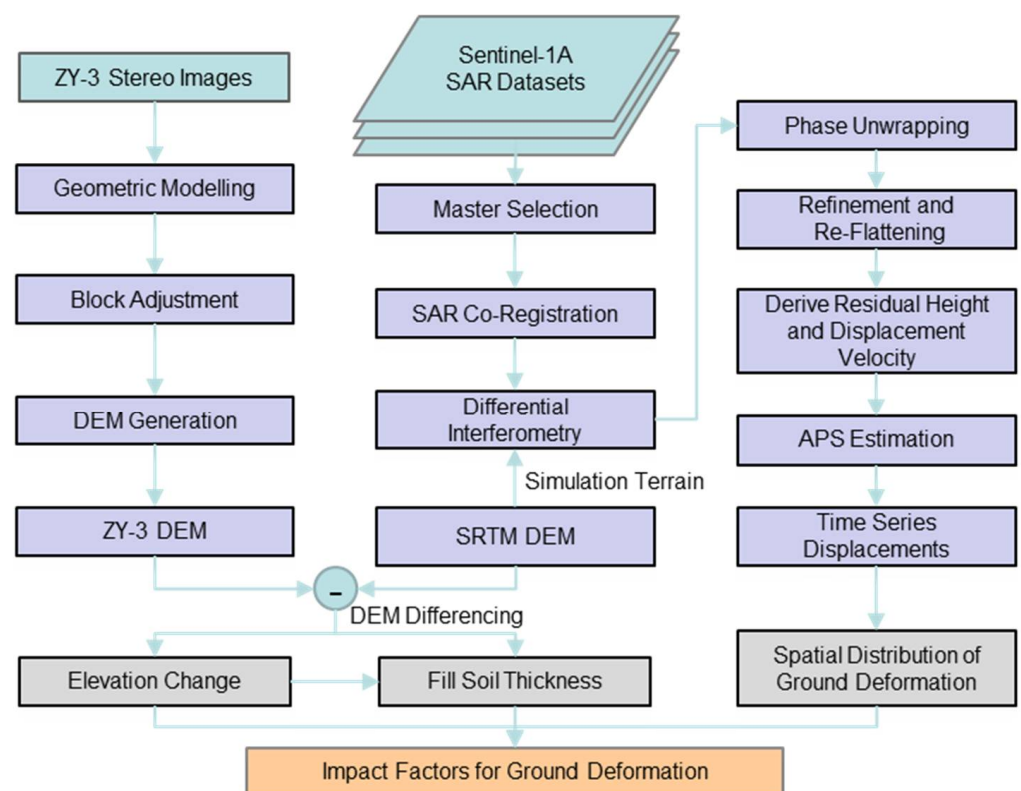


Figure 3. The methodology flowchart.

3.2.2. InSAR-Derived Deformation Rates

The conventional differential InSAR (D-InSAR) technique uses two SAR images obtained at different times and covers a common region to retrieve surface displacement from the phase differences detected during consecutive SAR acquisitions [35]. However, the precision of D-InSAR is always affected by several factors, such as spatial and temporal decorrelation, atmospheric artifacts [36], and an incorrect DEM. In order to mitigate the effects of these issues, advanced multitemporal InSAR techniques—such as SBAS-InSAR and PS-InSAR [20,21]—have been developed to detect ground displacements.

The SBAS-InSAR technique is an advanced InSAR time series analysis method that relies on multitemporal images to calculate ground deformation using interferometric pairs with shorter spatio-temporal baselines [22]. This technique effectively reduces the effects of spatial and/or temporal decorrelation and DEM errors on parameter estimation, which are common in the traditional D-InSAR processing technique [37]. SBAS-InSAR technology has been widely used for the monitoring of large-area surface deformation associated with anthropogenic activities, such as urbanization and groundwater extraction [5,9,38].

In order to acquire more reliable and higher-resolution time series deformation results in the land-creation area with a relatively high surface deformation rate, 32 scene Sentinel-1A images were processed using the SBAS-InSAR technique. First, all of the SAR images were accurately coregistered, and high-quality interferograms were generated based on small temporal and spatial baseline thresholds (less than 36 days and smaller than 100 m). External DEM data were utilized to simulate and remove the topographic phases. Then, multilooking and Goldstein filtering methods were applied in order to improve the signal-to-noise ratio and coherence of the interferograms. Phase unwrapping with the robust minimum cost flow (MCF) algorithm [39] was conducted on the coherent pixels for each wrapped interferogram.

The unwrapped interferometric phase at a pixel in the j th differential interferogram generated by two SAR images acquired at the start time t_A and end time t_B can be described as follows:

$$\delta\varphi_j = \varphi(t_B) - \varphi(t_A) \approx \delta\varphi_j^{def} + \delta\varphi_j^{topo} + \delta\varphi_j^{atm} + \delta\varphi_j^{noise} \quad (1)$$

where $\varphi(t_B)$ and $\varphi(t_A)$ are the phase signals at SAR acquisition dates t_A and t_B ($t_A < t_B$), respectively; $\delta\varphi_j^{def}$ represents the phase contributions from surface deformation along the line-of-sight (LOS) direction; $\delta\varphi_j^{topo}$ is the inaccurate DEM residual phase; $\delta\varphi_j^{atm}$ is the atmospheric phase caused by the difference in atmospheric delay between two observations; and $\delta\varphi_j^{noise}$ is the noise phase.

In order to improve the accuracy and reliability of the deformation results, these nuisance terms should be effectively estimated and eliminated from differential interferograms. The residual topographic phase can be estimated by utilizing its linear relationship with perpendicular baselines and the least squares method [40]. The atmospheric phase was estimated and subtracted from the interferometric phase by using a low-pass spatial filter and a high-pass temporal filter. Finally, the deformation velocity and time series deformation results were retrieved using the singular value decomposition (SVD) method after removing the abovementioned residual phase components from the interferometric phase. The detailed flowchart of the time series InSAR processing method is depicted in Figure 3.

4. Results and Analyses

4.1. Topographic Changes in YND

4.1.1. Spatial Evolution of the Topographic Changes

The visual interpretation of panchromatic ZY-3 images shows the history of land creation in the YND, as shown in Figure 4a–c. The corresponding topographic changes from 2000–2017 produced by differencing the ZY-3 and SRTM DEMs are shown in Figure 4A–C. The negative values in the map indicate a decrease in elevation (i.e., mountain excavation), and the positive values indicate an increase in elevation (i.e., valley filling). The land

creation produced elevation changes of up to 110 m in both the valley filling area and the mountain excavation area of the YND. Table 2 summarizes the fill thicknesses of the two main valley-filling areas. Generally, the spatial evolution of land creation and the corresponding topographic changes were clearly recorded, and three main stages could be roughly reflected. The first phase of land creation was completed before 17 November 2013, and was mainly concentrated in the Qiaoergou area, covering an area of approximately 10.6 km². The thickness of the filling loess in the Qiaoergou area ranges from 20 m to 60 m, with an average of 36 m and a maximum of approximately 110 m, which is generally consistent with previous reports [7]. The second phase aimed mainly to create land in the small watershed in the western part of the YND, with an additional land area of 8.2 km². The third phase of the land creation was completed on 13 October 2017, mainly in the lower reaches of the Gaojiagou gully. At this time, over 22.1 km² of flat land was created by the MECC project in the YND, including a 10.8 km² fill area. Notably, the land creation project in the northern part of the YND was still underway until it was fully completed in June 2018.

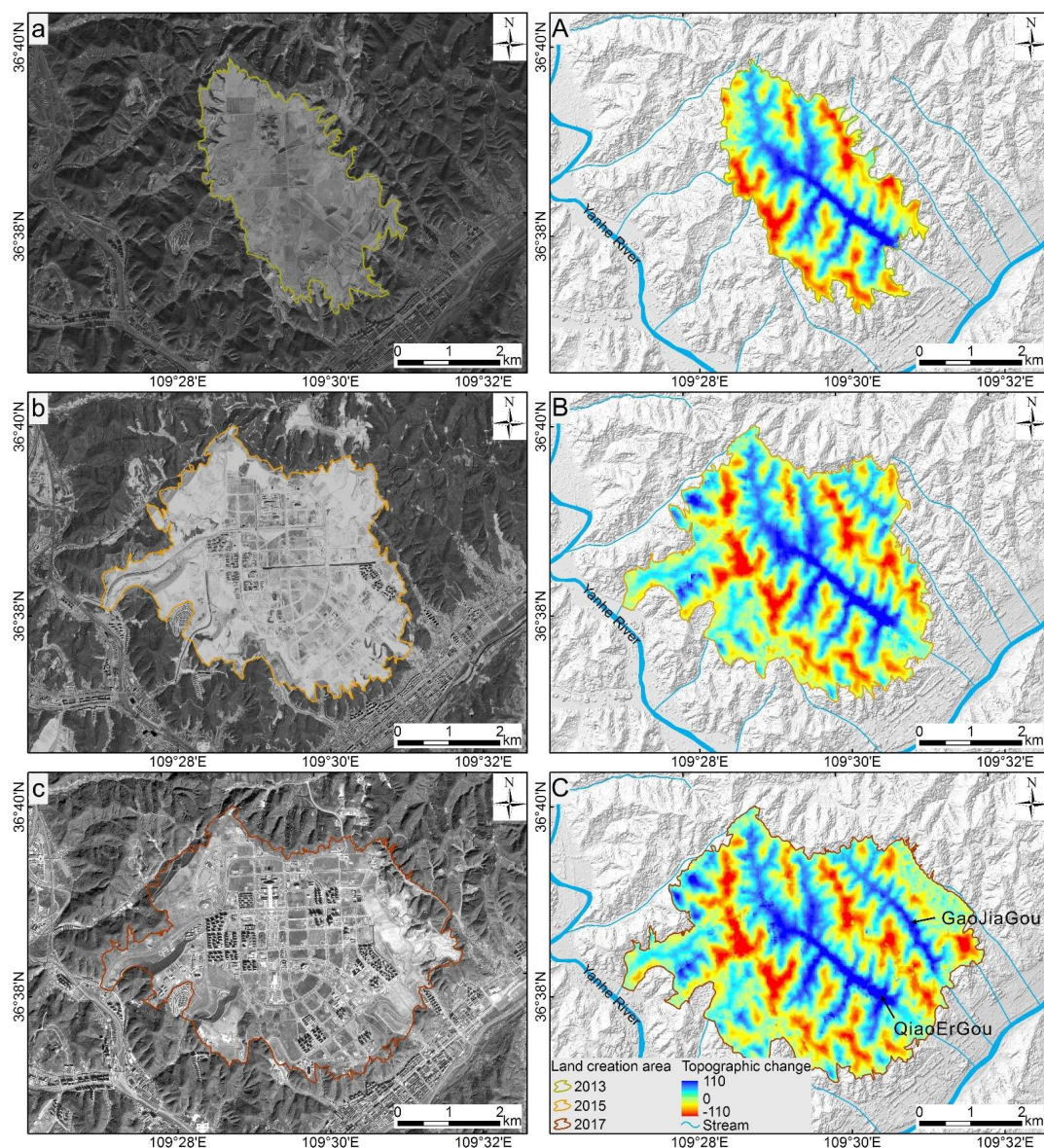


Figure 4. Spatial evolution of the land creation and the corresponding topographic changes in the YND. (a–c) History of the land creation revealed by the ZY-3 panchromatic images; (A–C) topographic changes in 2000–2013, 2000–2015 and 2000–2017 estimated by calculating the difference between the SRTM and the ZY-3 DEMs.

Table 2. The fill thicknesses for the two main valley-filling areas.

Land Creation Region	Completion Time	Fill Area (km ²)	Mean Thickness (m)	Maximum Thickness (m)
Qiaoergou	17 November 2013	5.9	36	108
Gaojiagou	13 October 2017	2.1	31	81

4.1.2. Uncertainty Characterization

The accuracy of the ZY-3 DEM was expressed as the mean and standard deviation of the elevation difference in the non-YND areas between the SRTM and ZY-3 DEMs from 2000 to 2017. Figure 5 delineates the difference map and the corresponding histogram of the elevation difference for the areas without land-creation work. The elevation differences are approximately normally distributed, and 65% of the rasters have absolute elevation differences less than 10 m. The mean value of the elevation difference is 3.7 m, while the standard deviation is 12.8 m. Compared with the excavation and filling of more than one hundred meters, this error has a limited impact on the estimation of the elevation changes in the YND. Basically, these statistical results show good agreement between the elevations of the two DEMs obtained from different sources. Some large local differences may be caused by various factors, such as the error contained in the preconstruction DEM, urban construction, gully land consolidation, and local land creation.

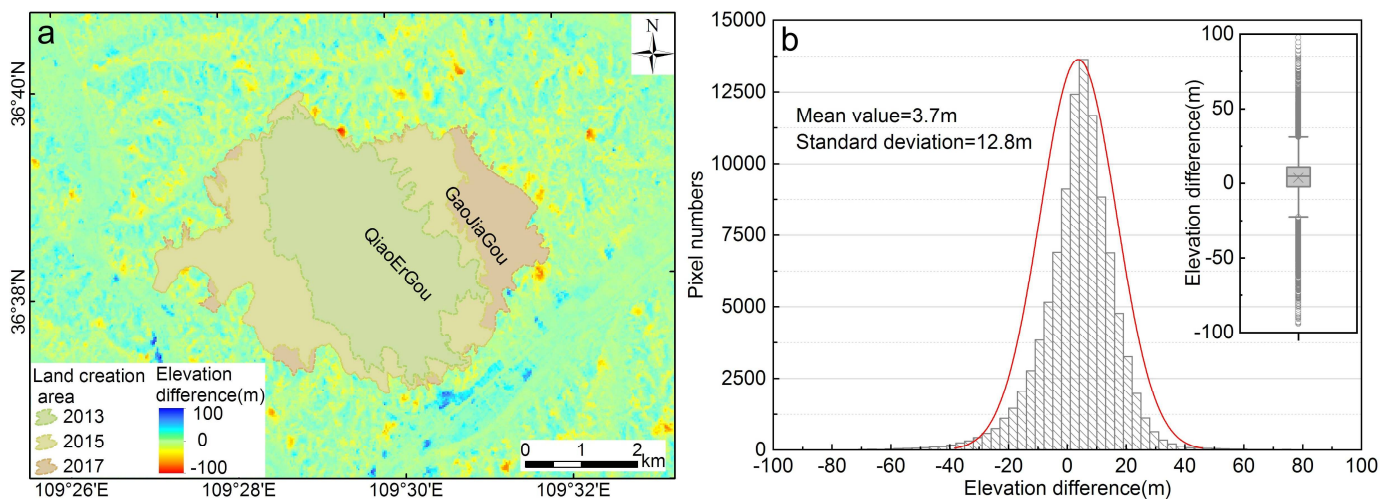


Figure 5. Elevation difference in non-YND areas between the SRTM and ZY-3 DEMs from 2000 to 2017; (b) the corresponding histogram of (a).

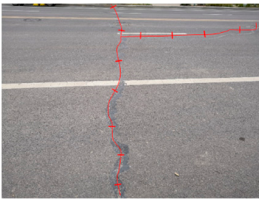
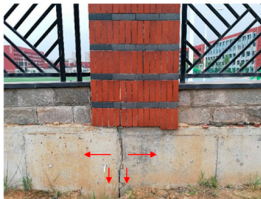
4.2. Ground Deformation of YND

4.2.1. Spatial Pattern

In this study, SBAS-InSAR technology was employed to quantify the spatiotemporal pattern of the surface deformation in the YND from December 2017 to December 2018. According to previous studies, the vertical deformation in the YND is much larger than the horizontal deformation, and is the main component of surface deformation [7]. In addition, due to the flat terrain of the YND, the LOS deformation acquired from InSAR technology was simply interpreted as vertical deformations in this study [27]. Figure 6 shows the maps of the LOS deformation rates measured by SBAS from Sentinel-1A data stacks. The red color (negative values) in Figure 6 indicates that the coherent targets (CTs) are moving away from the satellite (i.e., subsidence), while the green color (positive values) indicates movement toward the satellite (i.e., uplift). Selected areas with concentrated deformation rates below -10 mm/year were analyzed in order to grasp the characteristics of the land subsidence in the YND. Figure 6 shows that the entire area of the old city remained relatively stable during the whole monitoring period, with deformation rates

mainly in the range of -5 to 5 mm/year. However, there were approximately two regions located in the YND where severe subsidence was apparent, and the deformation rate was primarily in the range of -10 to -60 mm/year. These two major subsidence zones with high deformation rates are located in the central Qiaoergou region and Gaojiagou region (Figure 6).

Table 3. Examples of the ground deformation characteristics obtained from the field survey.

Location	P1	P2	P3	P4
Velocity (mm/yr)	-35.2	-20.1	-29.2	-23.7
Field investigation photos				

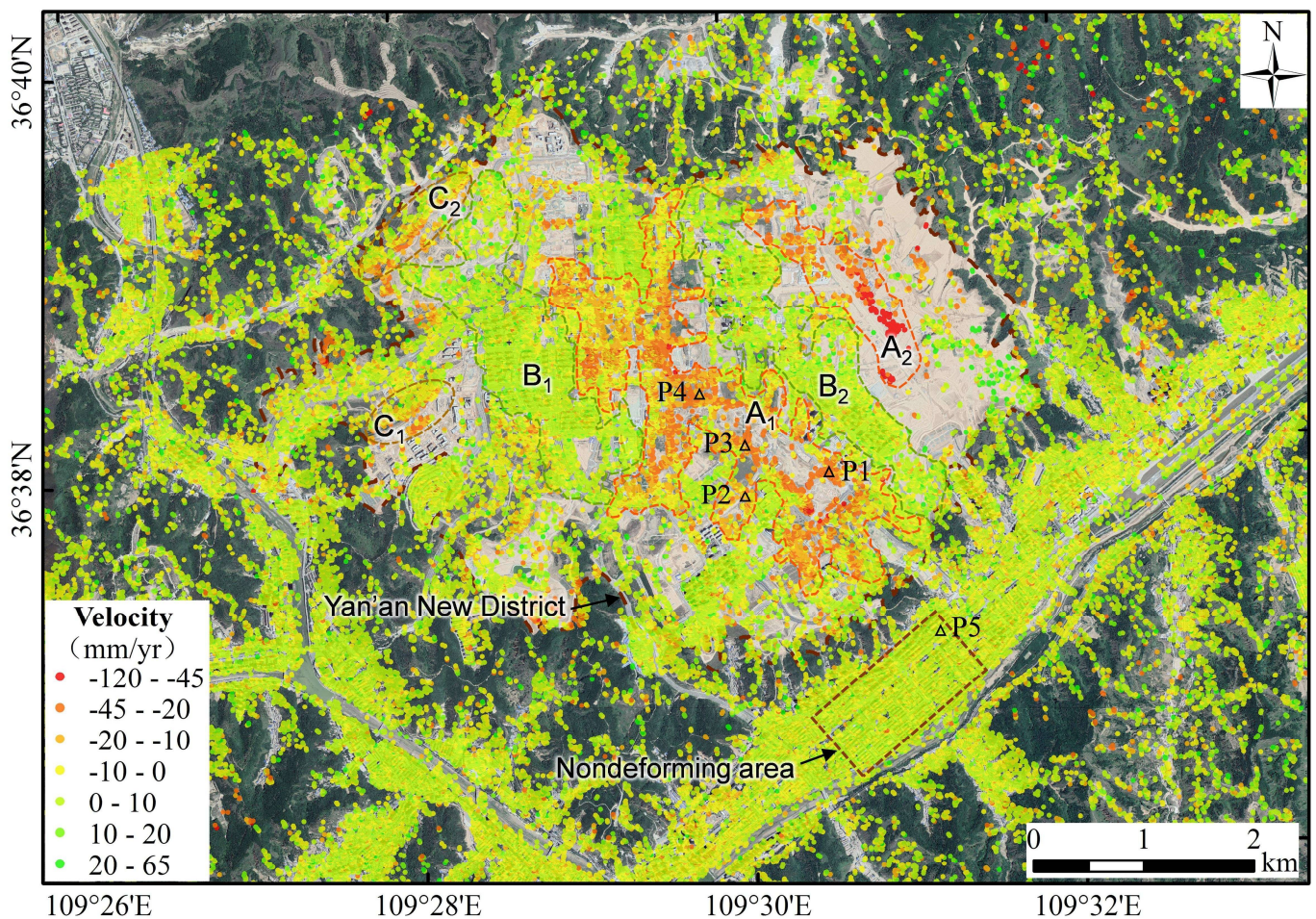


Figure 6. Annual deformation rates in the Yan'an New District. The dashed line outlines the main deformation area. The black triangles correspond to the four typical sample areas used in the field surveys and the time series analysis (see Table 3 and Figure 7).

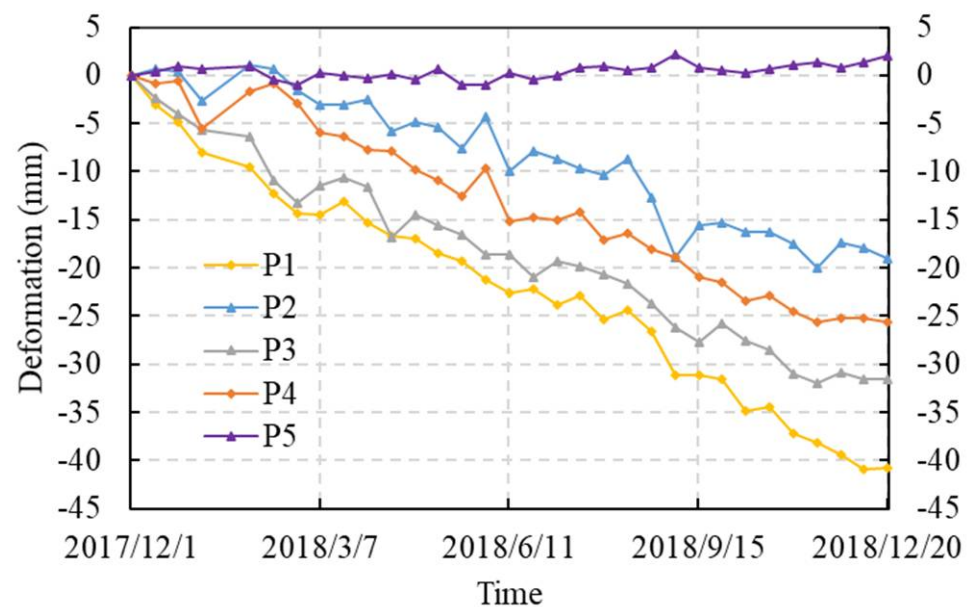


Figure 7. Accumulative time series deformation corresponding to feature points P1–P5, as marked in Figure 6.

The Qiaoergou region (i.e., Region A1) is in the major urban area of the YND. In this region, the severe land subsidence is distributed in a zone from northwest to southeast along the filling areas, with deformation rates ranging from -10 to -45 mm/year. The deformation rates increased gradually from the northwest to southeast of the subsidence zone. The largest subsidence was detected at the southeastern end of this land subsidence zone, with a maximum deformation rate up to -73 mm/year, which is consistent with the results derived from a previous study, e.g., 70 mm/year in 2015–2019 [5]. The central area of the Gaojiagou region (i.e., Region A2) is the second largest land subsidence zone in the YND, with a deformation rate ranging from -10 to -75 mm/year and a maximum value of -121 mm/year. However, very sparse measurement points were detected in the southeastern end of the Gaojiagou area, which is most likely due to the decoherence caused by continuous and high-intensity engineering activities, such as land creation and rapid construction.

In addition to the land subsidence in the filling region, large-scale uplift was also observed in the mountain excavation region (i.e., Regions B1 and B2), mainly ranging from 10 to 20 mm/year, with a maximum deformation rate of 62 mm/year, which might be attributed to the released load of the excavated mountains [5]. Additionally, some slight to moderate deformation areas were also observed in the engineering slope in the western part of the YND (i.e., Regions C1 and C2), which was continuously deformed from December 2017 to December 2018. The main deformation rate ranged from -10 to -30 mm/year, with a maximum deformation rate of -38 mm/year.

Since high-precision ground-based levelling data were unavailable in this region, a series of detailed field investigations were conducted in April 2019 in order to verify the accuracy and reliability of the InSAR-derived deformation results. Table 3 shows the ground deformation characteristics obtained from the field survey based on the InSAR-derived deformation results. The locations of the field investigation photos are marked by black triangles in Figure 6. As seen in Table 3, a series of ground deformation occurrences—such as road cracks and wall cracks—are distributed on the YND, which is consistent with the InSAR-derived results. For the Qiaoergou region, due to the gradual improvement of the infrastructure and major roads, the ground deformation characteristics in this region are more obvious than those in the Gaojiagou region, such as road pavement cracks, wall cracks, and surface drainage channel cracks (Table 3). However, in the Gaojiagou region,

the completion time of the land creation project was relatively late, and there are almost no buildings; the area is mainly covered by woodland or wasteland. Therefore, although the ground deformation rate in this area is higher than that in the Qiaoergou region, the signs of deformation failure on the site are not obvious, and there is only obvious damage in the flood control ponds. Overall, good agreement between InSAR-derived results and field survey data was obtained, which suggests that the SBAS method can achieve reliable and accurate surface deformation measurements for land-creation areas. Additionally, the standard deviation of the InSAR results over a known nondeforming area (orange rectangle in Figure 6) was calculated as an indicator to further quantify the accuracy of our results. The standard deviation is approximately 4.3 mm/year, indicating that the InSAR measurements have reliable accuracy.

4.2.2. Temporal Evolution

The SBAS-InSAR method allowed for the temporal deformation evolution estimation for each of the CTs identified in the SAR imagery. Thus, we selected the four field survey points (P1 to P4) mentioned above on different parts of the YND, as well as a stable reference point P5 in the old city, as marked with triangles in Figure 6, in order to quantitatively analyze the temporal evolution of the ground deformation. The time series of the deformation from December 2017 to December 2018 measured by the Sentinel-1A data stacks is shown in Figure 7. A negative value indicates that the ground target was moving away from the satellite. The temporal evolution of the deformation at the four feature points (P1 to P4) shows similar near-linear trends with various velocities. P5—located in the old urban area—is basically stable, with a cumulative deformation within 2 mm during the whole monitoring period. The cumulative deformation of the four feature points (P1 to P4) exceeds 20 mm in only one year, which is enough to trigger and aggravate road pavement cracks and wall cracks (Table 3). The maximum and minimum accumulative deformations were observed at P1 and P2, with magnitudes of -41 and -20 mm, respectively. Notably, the subsidence at P1 to P4 still exhibited a large subsidence trend and deformation rate, which suggested that the YND will still undergo significant land subsidence in the near future. Therefore, long-term, multiscale ground monitoring is required in order to further understand the detailed temporal evolution of the subsidence.

4.3. Relationships between the Topographic Changes and Land Subsidence

As mentioned earlier, the large-scale land creation caused significant topographic changes, forming large loess high-fill foundations with a maximum thickness of 110 m. The results of the previous stratified settlement monitoring showed that the settlement of the underlying original loess in the YND mainly occurred during the construction period, while the postconstruction ground settlement mainly consisted of fill body compression [7]. Therefore, the distribution and thickness of the filling body had a significant effect on the distribution and magnitude of the land subsidence. The fill thickness contour lines were spatially analyzed with InSAR-derived deformation information, as shown in Figure 8. It is clear from Figure 8 that the InSAR-derived deformation pattern over the YND shows a high correlation between the detected subsidence and the thickness of the filling loess. In areas with large difference values in fill thickness, significant land subsidence differences can be identified. Moreover, relatively high subsidence rates (>20 mm/year) were observed in the center of the Qiaoergou and Gaojiagou regions, which are characterized by a relatively greater thickness of filling loess.

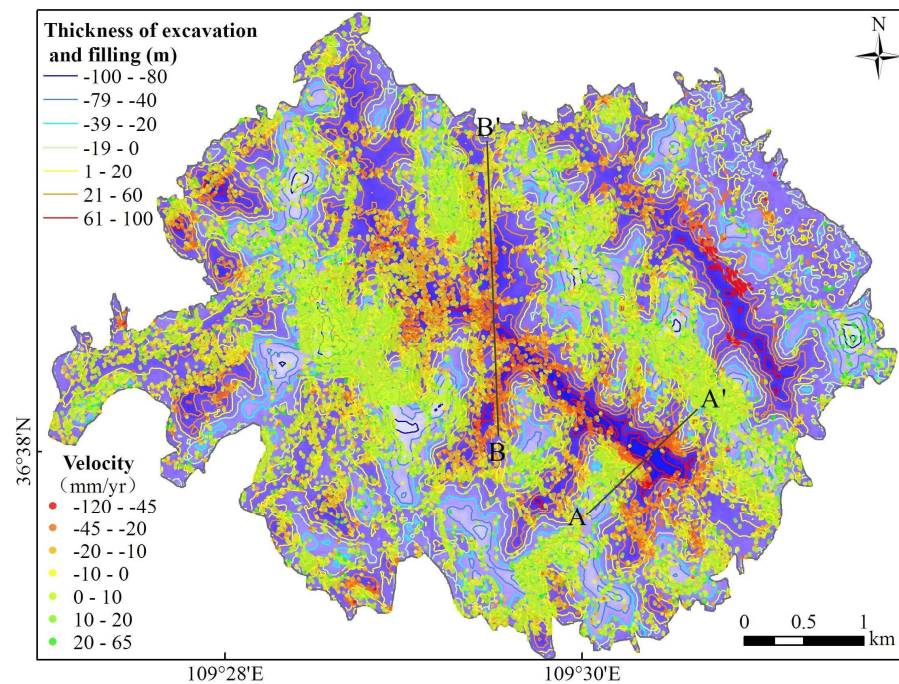


Figure 8. Relationship between the thickness of the filling loess and the subsidence in the YND. The InSAR-derived ground deformations (scatter) are superimposed on the thickness contours of the excavation and filling. The negative value of the contour line represents the excavation, and the positive value represents the filling. The solid black line indicates the profile lines in Figure 9.

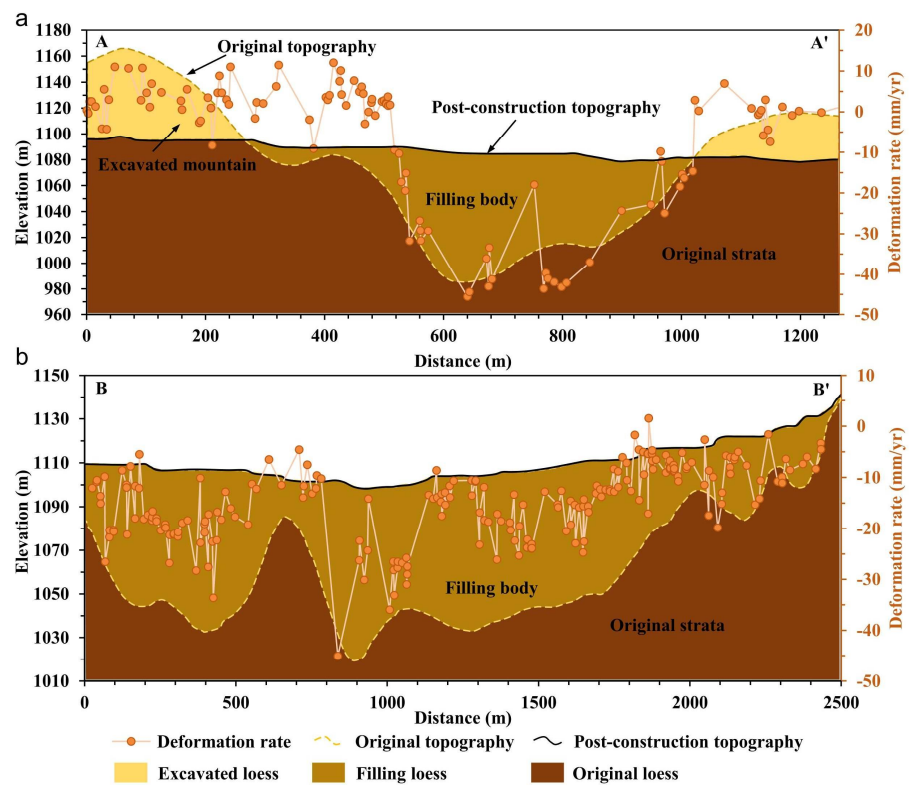


Figure 9. Comparison of the subsidence with the thickness of filling loess along two profiles of which the positions are marked in Figure 8. A negative deformation means subsidence.

In order to further investigate the spatial correlation between the topographic changes and land subsidence, the elevation and deformation rates along profiles AA' and BB'

were extracted, as shown in Figure 9. Profile AA' crosses the bottom of the Qiaoergou gully almost vertically. The subsidence along the profile increases with the increase in the fill thickness. The maximum deformation rate along the profile was approximately 45.6 mm/year, which is located in the middle of the profile with the largest thickness of filled loess. Profile BB' extends from the middle to the top of the Qiaoergou gully in a north–south direction. A similar phenomenon can be found in this profile, in which the maximum deformation is observed at the maximum filling loess thickness. In general, the subsidence rate is higher at positions with a greater thickness of filling loess, which indicates that the subsidence formed by the compression of the filling loess is relatively large under self-compression and external loading, because the filling loess is highly compressible.

In order to quantitatively determine the correlation between the fill thickness and the land subsidence, the fill thickness at each CT in the Qiaoergou region was extracted and then statistically analyzed. Figure 10a presents the percentage of CTs with different deformation rates in different fill thicknesses. Almost all of the ground subsidence (94.7% of the total CTs with deformation rates below -10 mm/year) is concentrated in the area where the thickness of the fill is greater than 30 m. Moreover, as the thickness of the fill increases, the proportion of CTs with higher subsidence rates increases significantly; in particular, subsidence at rates exceeding 50 mm/year was only observed in the area where the thickness of the fill is greater than 70 m. In contrast, no subsidence or minor subsidence was observed in areas with low fill thickness, especially below 20 m. Figure 10b presents the average subsidence rate for different fill thicknesses. A positive correlation between the subsidence rate and the fill thickness was observed; that is, the subsidence rate increases significantly with increasing filling loess thicknesses. These phenomena suggest that the different magnitudes of land subsidence after land creation are largely controlled by the compaction process of the filling loess with different thicknesses.

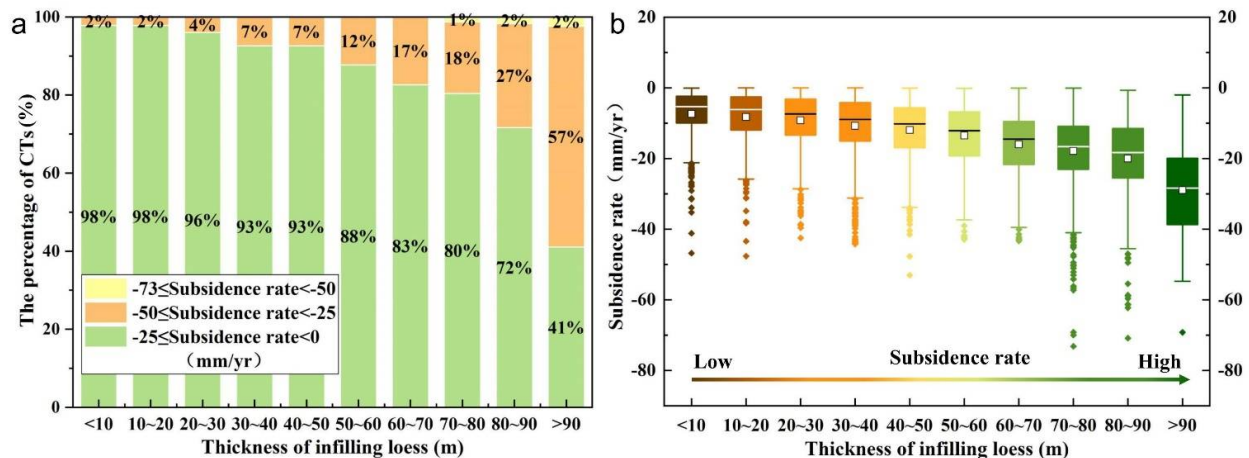


Figure 10. A quantitative relationship between the subsidence and filling thickness. (a) Statistics of the CTs for different thicknesses of infilling loess; (b) statistics of the deformation rates for different thicknesses of infilling loess.

5. Discussion

5.1. Subsidence and the MECC Project

5.1.1. Effect of Large-Scale Land Creation and Urban Construction

Figure 11 shows the overlap between the ground deformation, the land-creation area, and the construction area. Clearly, there was an obvious high spatial correlation between the surface deformation and the land creation, indicating a high level of spatial control of the subsidence by the land creation. The density of the total CTs distributed in the non-filled area is 1482/km², while it decreased to 1191/km² in the filled area, which is mainly caused by the SAR image resolution and continuous engineering activities. However, the density of the CTs distributed in the filled area with deformation rates below

−10 mm/year (indicating subsidence) reached 616/km², while it decreased to 163/km² in the non-filled area.

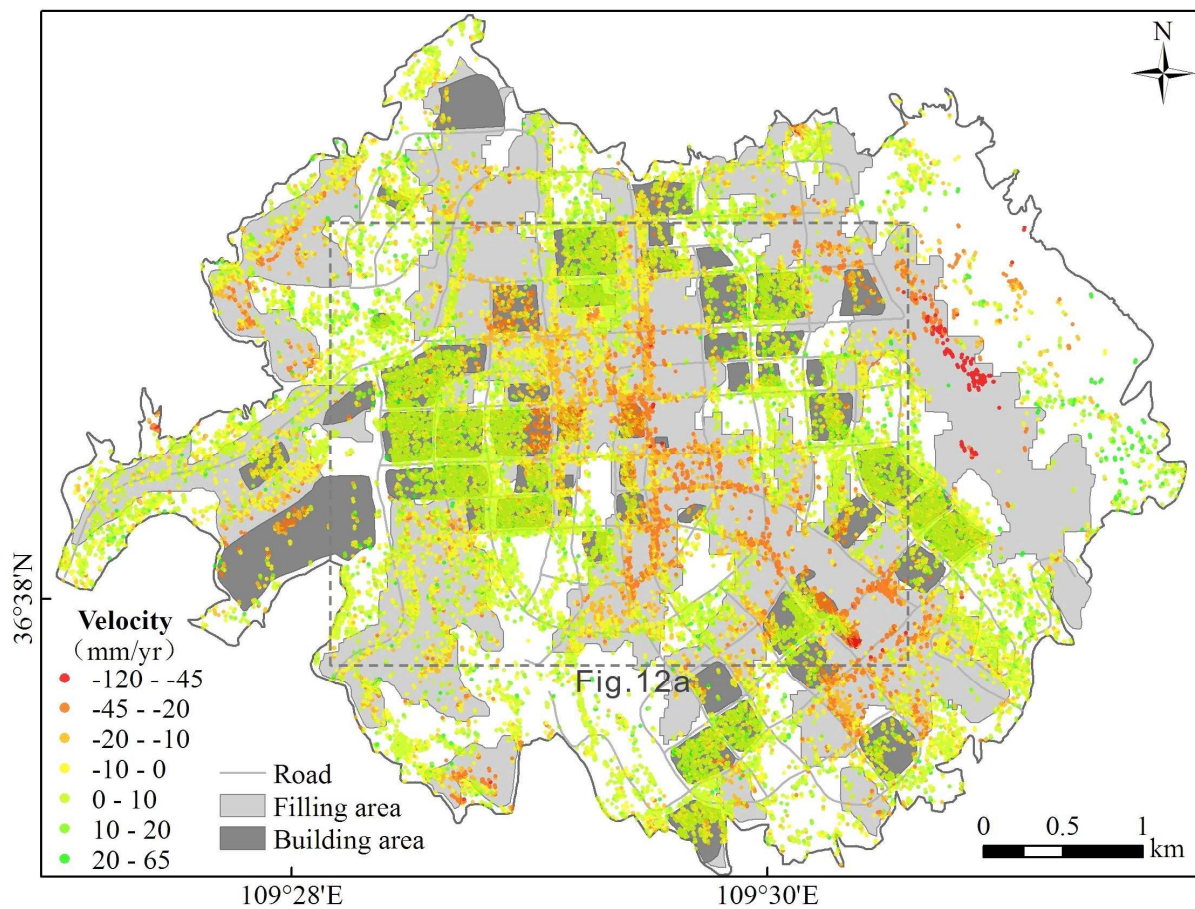


Figure 11. Land creation and urban construction in relation to the subsidence in the YND. The rectangular box is enlarged and shown in Figure 12.

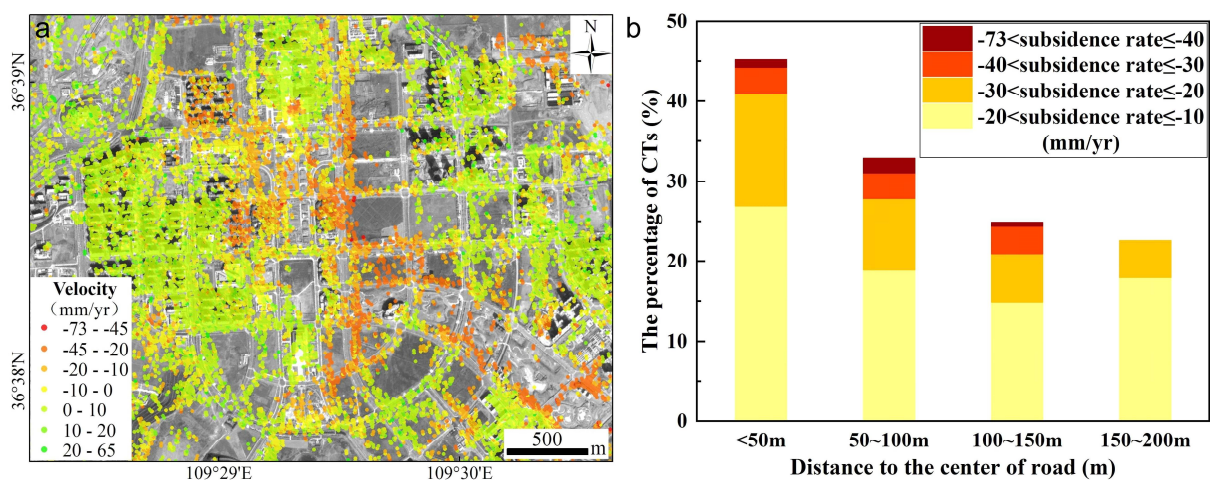


Figure 12. Relationship between the land subsidence and road networks. (a) Enlarged deformation map of the area in the rectangle in Figure 11. The background is a panchromatic ZY-3 image. (b) Statistics of the CTs at different distances from the road.

In addition, more than 81% of the total CTs with deformation rates below −10 mm/year (indicating subsidence) are concentrated in the infilling area, with a maximum deformation

rate of -121 mm/year, which indicates that most of the land subsidence in the YND occurred in the filling area. On the other hand, there is a relatively weak correlation in the spatial distribution between the land subsidence and buildings. Generally, only 15.86% of the total CTs indicating subsidence are distributed in the building area, whereas 54.82% of these buildings are localized within the filled area. Compared with land creation, building construction has a significantly smaller impact on ground settlement, mainly because most of the building construction is located in relatively stable excavation areas. Therefore, it is not difficult to see that the spatial pattern of the land subsidence over the YND is bounded and controlled by large-scale land creation. Filled loess is formed by the remodeling and backfilling of original loess during filling work, which has a loose structure and weak mechanical properties. Therefore, in the land-creation area, especially the filling area, the loess-filled foundation is prone to compaction under its own weight and external load, which finally leads to significant subsidence.

5.1.2. Relationship between the Land Subsidence and Road Network

Notably, the observed subsidence can also be affected by effects relevant to road construction. As of June 2018, the total length of the road network in the YND exceeded 80 km (Figure 11), with a distribution density of 3.64 km/km², which had a significant impact on the development of the subsidence. Figure 12a shows that there is a strong spatial correlation between the observed subsidence and the dense road network. Severe land subsidence was observed along the road networks, which was consistent with road pavement cracks during the field survey (Table 3). Thus, subsidence is a major threat to vehicle safety.

For a further analysis of the spatial distribution relationship between the road network and the land subsidence, CTs at different distances from the center of the road were selected for the Qiaoergou filling area as an example, and then a statistical analysis of the subsidence rates corresponding to these CTs was executed. Figure 12b indicates the percentage of the number of largely-subsiding CTs compared to the total number of CTs within different distance ranges. In Figure 12b, the proportion of CTs with higher subsidence rates to the total number of CTs increases significantly as the distance from the center of the road decreases, indicating that the land subsidence around the center of the road is more significant. On the contrary, relatively slight land subsidence occurs only in the areas with larger distances from the center of the road, especially those larger than 150 m, suggesting that the ground deformation in this area is mainly caused by the natural consolidation process of the filled loess. This result indicates that the land subsidence in the YND is also somewhat affected by road construction. The long-term cyclic traffic load and its vibration load due to the dense road network will accelerate the consolidation process of the filling loess, thereby significantly exacerbating the progression of the land subsidence.

5.2. Natural Drivers of Subsidence

A complex geological environment is often an important factor that impacts land subsidence [41]. As mentioned earlier, almost all of the land subsidence occurred in the infilling area. The compressible and collapsible deformation of the filled loess may be the potential mechanism of large-scale land subsidence in the YND. Large-scale land creation, including the excavation of loess hills to fill valleys, will potentially modify the geotechnical properties (such as the collapsibility and compressibility) of the original loess [38]. Therefore, in the infilling area, the infilling loess has the properties of weak cementation and a relatively loose structure [42], which makes it easy to experience substantial compression under the action of self-weight or an external load. In addition, many studies have shown that repeated loess compaction in layers during the filling work is not enough to completely remove the threat of the loess foundation's collapse. Conversely, the collapsibility of the compacted loess is even more serious than that of intact loess [38,43]. Therefore, under external loads (engineering vehicles and heavy buildings) and wetting (rainfall or irrigation), filling loess is more prone to compaction and collapsible deformation, ultimately

leading to substantial land subsidence. In summary, considering the significant influence of the surface geological characteristics on the subsidence rate and magnitude, the spatial variability in filled loess in terms of thickness and lithological characteristics of soils largely determines the spatiotemporal pattern of the land subsidence in the YND [12,44].

5.3. Implications and Limitations

In this study, the InSAR-derived results showed that YND suffered a maximum subsidence deformation of more than 120 mm in only one year, which posed a great challenge to the urban construction of the YND. Severe land subsidence not only threatens the safety of buildings and infrastructures but also greatly restricts the application of the MECC project in the YND, and even affects the sustainable development of the city. Moreover, given the large-scale land creation, increasing urbanization of the YND and the related increase in external loads from high-rise buildings and traffic networks, the infilling loess is more prone to compaction and, eventually, accelerated subsidence [38]. Accordingly, the extensive research efforts on the postconstruction subsidence estimation and prediction should be continued and accelerated in the aspects of geological interpretation, geotechnical investigation, ground monitoring and modeling, and InSAR observation. Furthermore, InSAR analysis has been demonstrated to be a valuable tool for mapping land subsidence, which should be taken into account in future urbanization planning and technical solutions involved in avoiding infrastructure damage caused by subsidence [27]. Finally, the ongoing monitoring of land-creation areas is needed in order to update the information on the compression or consolidation of filling loess, and to identify early critical situations that may cause damage to the urban infrastructures in these areas [27]. Fortunately, our results indicate that the planning and construction in the YND are generally consistent with the rules for land creation construction in the YND, where construction work will be carried out first in the mountain excavation region and will not expand into the infilled areas until the ground stabilizes by natural settlement [45].

In this paper, the rates and patterns of postconstruction land deformation associated with MECC in the YND were investigated using advanced time series InSAR analysis combined with topographic change and optical remote sensing data; however, several limitations remain. These limitations consist in the lack of valid in situ measurements, such as levelling data and the latest monitoring well data, which would provide a powerful validation of the subsidence rates and patterns, and would be of assistance in urban planning and land subsidence mitigation.

In the near future, various in situ measurement data, such as ground and deep monitoring data, groundwater level changes, and geotechnical data, will be collected, and a further joint analysis of multidisciplinary data will be conducted in order to comprehensively understand the complex subsidence phenomena in the YND. This action will enable us to thoroughly understand the spatiotemporal evolution and mechanism of land subsidence in order to ensure the reliability of the long-term subsidence predictions and thereby assist decision making on land subsidence mitigation.

6. Conclusions

In this study, the local topographic changes and ground deformation caused by the large-scale MECC project in the YND, as well as their interactions, were investigated by jointly using space-borne optical photogrammetry, time series InSAR techniques, remote sensing images, and field surveys. First, new surface elevations were extracted from ZY-3 stereo images using space-borne optical photogrammetry, and then the topographic changes and fill thickness associated with the MECC project between 2000 and 2017 were derived from the ZY-3 DEM and SRTM DEM using the geodetic method. By October 2017, over 22 km² of flat land, including 10.8 km² of filled area, was created, with a maximum filling depth of approximately 110 m. Second, the ground deformation after the MECC project was retrieved by applying the SBAS-InSAR technique using the Sentinel-1 SAR dataset. Extensive land subsidence, with a maximum settlement rate of 121 mm/year,

was detected in the land-creation area, which is consistent with the detailed field findings. Finally, the quantitative analysis of various driving forces of subsidence was conducted by combining the InSAR results with engineering activities, local geological data, and remote sensing data. Large-scale land creation determines the spatial and temporal patterns of land subsidence, while the thickness of the filled loess controls the magnitude of the land subsidence, and human activities, as well as changes in the geological environment, will also accelerate the process of subsidence. These results demonstrate that long-term, multiscale deformation monitoring is needed in order to update the information regarding the compression or consolidation of filling loess, thus ensuring the safe operation and sustainability of the MECC project.

Author Contributions: Conceptualization, C.P. and Q.X.; methodology, C.P.; formal analysis, K.Z. and Y.J.; data curation, L.H.; writing—original draft preparation, C.P., investigation, J.L.; visualization, W.C.; funding acquisition, Q.X.; validation, P.K. All authors have read and agreed to the published version of the manuscript.

Funding: This research was funded by the National Natural Science Foundation of China (Grant No. 41790445, 41630640), the Key Research and Development Program of Sichuan Province (2020YFS0353), the Open Fund of State Key Laboratory of Geohazard Prevention and Geoenvironment Protection (Grant No. SKLGP2017K016), and the Science Fund for Creative Research Groups of the National Natural Science Foundation of China (Grant No. 41521002).

Acknowledgments: We are grateful to the European Space Agency for providing the Sentinel-1A data freely. We also thank the three anonymous reviewers and the editor for their constructive comments and suggestions, which have significantly improved this paper.

Conflicts of Interest: The authors declare no conflict of interest.

Abbreviations

MECC: Mountain Excavation and City Construction; YND, Yan'an New District; ZY-3, Ziyuan-3; InSAR, interferometric synthetic aperture radar; SBAS, small baseline subset; GPS, global positioning system; DEM, digital elevation model; SRTM, Shuttle Radar Topography Mission, TLA, three-line-array; RFM, rational functional model; RPC, rational polynomial coefficient; GCP, ground control points; LOS, line-of-sight; CT, coherent target.

References

1. Liu, T. *Loess and the Environment*; Science Press: Beijing, China, 1985. (In Chinese)
2. Li, P.; Qian, H.; Wu, J. Accelerate research on land creation. *Nature* **2014**, *510*, 29–31. [[CrossRef](#)] [[PubMed](#)]
3. Kou, P.; Xu, Q.; Yunus, A.P.; Dong, X.; Pu, C.; Zhang, X.; Jin, Z. Micro-topographic assessment of rill morphology highlights the shortcomings of current protective measures in loess landscapes. *Sci. Total Environ.* **2020**, *737*, 139721–139731. [[CrossRef](#)] [[PubMed](#)]
4. Chen, W.; Xu, Q.; Zhao, K.; Zhou, X.; Li, S.; Wang, J.; Wang, X.; Xu, J. Spatial analysis of land-use management for gully land consolidation on the Loess Plateau in China. *Ecol. Indic.* **2020**, *117*, 106633–106649. [[CrossRef](#)]
5. Wu, Q.; Jia, C.; Chen, S.; Li, H. SBAS-InSAR based deformation detection of urban land, created from mega-scale mountain excavating and valley filling in the Loess Plateau: The case study of Yan'an City. *Remote Sens.* **2019**, *11*, 1673. [[CrossRef](#)]
6. Juang, C.H.; Dijkstra, T.; Wasowski, J.; Meng, X. Loess geohazards research in China: Advances and challenges for mega engineering projects. *Eng. Geol.* **2019**, *251*, 1–10. [[CrossRef](#)]
7. Ge, M.; Li, N.; Zhang, W.; Zheng, J.; Zhu, C. Settlement behavior and inverse prediction of post-construction settlement of high filled loess embankment. *Chin. J. Rock Mech. Eng.* **2017**, *36*, 745–753. [[CrossRef](#)]
8. Guo, L.; Li, J.; Li, Z.W.; Wu, L.X.; Li, X.; Hu, J.; Li, H.L.; Li, H.Y.; Miao, Z.L.; Li, Z.Q. The Surge of the Hispar Glacier, Central Karakoram: SAR 3-D Flow Velocity Time Series and Thickness Changes. *J. Geophys. Res. Solid Earth* **2020**, *125*, 1–24. [[CrossRef](#)]
9. Rateb, A.; Abotalib, A.Z. Inferencing the land subsidence in the Nile Delta using Sentinel-1 satellites and GPS between 2015 and 2019. *Sci. Total Environ.* **2020**, *729*, 138868. [[CrossRef](#)] [[PubMed](#)]
10. Xu, Q.; Zhao, K.; Liu, F.; Peng, D.; Chen, W. Effects of land use on groundwater recharge of a loess terrace under long-term irrigation. *Sci. Total Environ.* **2021**, *751*, 142340–142354. [[CrossRef](#)] [[PubMed](#)]
11. Ren, S.; Menenti, M.; Jia, L.; Zhang, J.; Zhang, J.; Li, X. Glacier mass balance in the Nyainqentanglha mountains between 2000 and 2017 retrieved from ZiYuan-3 stereo images and the SRTM DEM. *Remote Sens.* **2020**, *12*, 864. [[CrossRef](#)]

12. Ma, P.; Wang, W.; Zhang, B.; Wang, J.; Shi, G.; Huang, G.; Chen, F.; Jiang, L.; Lin, H. Remotely sensing large- and small-scale ground subsidence: A case study of the Guangdong–Hong Kong–Macao Greater Bay Area of China. *Remote Sens. Environ.* **2019**, *232*, 111282–111299. [[CrossRef](#)]
13. Yang, C.; Lu, Z.; Zhang, Q.; Zhao, C.; Peng, J.; Ji, L. Deformation at longyao ground fissure and its surroundings, north China plain, revealed by ALOS PALSAR PS-InSAR. *Int. J. Appl. Earth Obs. Geoinf.* **2018**, *67*, 1–9. [[CrossRef](#)]
14. Atzori, S.; Antonioli, A.; Tolomei, C.; De Novellis, V.; De Luca, C.; Monterroso, F. InSAR full-resolution analysis of the 2017–2018 M>6 earthquakes in Mexico. *Remote Sens. Environ.* **2019**, *234*, 111461–111470. [[CrossRef](#)]
15. Confuorto, P.; Di Martire, D.; Infante, D.; Novellino, A.; Papa, R.; Calcaterra, D.; Ramondini, M. Monitoring of remedial works performance on landslide-affected areas through ground- and satellite-based techniques. *Catena* **2019**, *178*, 77–89. [[CrossRef](#)]
16. Li, M.; Zhang, L.; Ding, C.; Li, W.; Luo, H.; Liao, M.; Xu, Q. Retrieval of historical surface displacements of the Baige landslide from time-series SAR observations for retrospective analysis of the collapse event. *Remote Sens. Environ.* **2020**, *240*, 111695–111705. [[CrossRef](#)]
17. Carlà, T.; Intrieri, E.; Raspini, F.; Bardi, F.; Farina, P.; Ferretti, A.; Colombo, D.; Novali, F.; Casagli, N. Perspectives on the prediction of catastrophic slope failures from satellite InSAR. *Sci. Rep.* **2019**, *9*, 14137–14145. [[CrossRef](#)] [[PubMed](#)]
18. Cigna, F.; Tapete, D. Present-day land subsidence rates, surface faulting hazard and risk in Mexico City with 2014–2020 Sentinel-1 IW InSAR. *Remote Sens. Environ.* **2021**, *253*, 112161–112179. [[CrossRef](#)]
19. Colesanti, C.; Ferretti, A.; Prati, C.; Rocca, F. Monitoring landslides and tectonic motions with the Permanent Scatterers Technique. *Eng. Geol.* **2003**, *68*, 3–14. [[CrossRef](#)]
20. Ferretti, A.; Prati, C.; Rocca, F. Permanent scatterers in SAR interferometry. *IEEE Trans. Geosci. Remote Sens.* **2001**, *39*, 8–20. [[CrossRef](#)]
21. Ferretti, A.; Prati, C.; Rocca, F. Nonlinear subsidence rate estimation using permanent scatterers in differential SAR interferometry. *IEEE Trans. Geosci. Remote Sens.* **2000**, *38*, 2202–2212. [[CrossRef](#)]
22. Berardino, P.; Fornaro, G.; Lanari, R.; Sansosti, E. A new algorithm for surface deformation monitoring based on small baseline differential SAR interferograms. *IEEE Trans. Geosci. Remote Sens.* **2002**, *40*, 2375–2383. [[CrossRef](#)]
23. Castellazzi, P.; Garfias, J.; Martel, R.; Brouard, C.; Rivera, A. InSAR to support sustainable urbanization over compacting aquifers: The case of Toluca Valley, Mexico. *Int. J. Appl. Earth Obs. Geoinf.* **2017**, *63*, 33–44. [[CrossRef](#)]
24. Figueroa-Miranda, S.; Tuxpan-Vargas, J.; Ramos-Leal, J.A.; Hernández-Madrigal, V.M.; Villaseñor-Reyes, C.I. Land subsidence by groundwater over-exploitation from aquifers in tectonic valleys of Central Mexico: A review. *Eng. Geol.* **2018**, *246*, 91–106. [[CrossRef](#)]
25. Corbau, C.; Simeoni, U.; Zoccarato, C.; Mantovani, G.; Teatini, P. Coupling land use evolution and subsidence in the Po Delta, Italy: Revising the past occurrence and prospecting the future management challenges. *Sci. Total Environ.* **2019**, *654*, 1196–1208. [[CrossRef](#)]
26. Solari, L.; Ciampalini, A.; Raspini, F.; Bianchini, S.; Moretti, S. PSInSAR analysis in the pisa urban area (Italy): A case study of subsidence related to stratigraphical factors and urbanization. *Remote Sens.* **2016**, *8*, 120. [[CrossRef](#)]
27. Hu, L.; Dai, K.; Xing, C.; Li, Z.; Tomás, R.; Clark, B.; Shi, X.; Chen, M.; Zhang, R.; Qiu, Q.; et al. Land subsidence in Beijing and its relationship with geological faults revealed by Sentinel-1 InSAR observations. *Int. J. Appl. Earth Obs. Geoinf.* **2019**, *82*, 101886–101895. [[CrossRef](#)]
28. Yu, H.; Gong, H.; Chen, B.; Liu, K.; Gao, M. Analysis of the influence of groundwater on land subsidence in Beijing based on the geographical weighted regression (GWR) model. *Sci. Total Environ.* **2020**, *738*, 139405–139418. [[CrossRef](#)] [[PubMed](#)]
29. Qu, F.; Zhang, Q.; Lu, Z.; Zhao, C.; Yang, C.; Zhang, J. Land subsidence and ground fissures in Xi’an, China 2005–2012 revealed by multi-band InSAR time-series analysis. *Remote Sens. Environ.* **2014**, *155*, 366–376. [[CrossRef](#)]
30. Wang, T.; Zhang, G.; Li, D.; Tang, X.; Jiang, Y.; Pan, H.; Zhu, X.; Fang, C. Geometric accuracy validation for ZY-3 satellite imagery. *IEEE Geosci. Remote Sens. Lett.* **2014**, *11*, 1168–1171. [[CrossRef](#)]
31. Dong, Y.; Chen, W.; Chang, H.; Zhang, Y.; Feng, R.; Meng, L. Assessment of orthoimage and DEM derived from ZY-3 stereo image in Northeastern China. *Surv. Rev.* **2016**, *48*, 247–257. [[CrossRef](#)]
32. Ni, W.; Sun, G.; Ranson, K.J.; Pang, Y.; Zhang, Z.; Yao, W. Extraction of ground surface elevation from ZY-3 winter stereo imagery over deciduous forested areas. *Remote Sens. Environ.* **2015**, *159*, 194–202. [[CrossRef](#)]
33. Zhou, P.; Tang, X.; Wang, Z.; Cao, N.; Wang, X. Vertical accuracy effect verification for satellite imagery with different GCPs. *IEEE Geosci. Remote Sens. Lett.* **2017**, *14*, 1268–1272. [[CrossRef](#)]
34. Soliman, A.; Han, L. Effects of vertical accuracy of digital elevation model (DEM) data on automatic lineaments extraction from shaded DEM. *Adv. Space Res.* **2019**, *64*, 603–622. [[CrossRef](#)]
35. Zhang, Y.; Meng, X.M.; Dijkstra, T.A.; Jordan, C.J.; Chen, G.; Zeng, R.Q.; Novellino, A. Forecasting the magnitude of potential landslides based on InSAR techniques. *Remote Sens. Environ.* **2020**, *241*, 111738–111751. [[CrossRef](#)]
36. Wasowski, J.; Bovenga, F. Investigating landslides and unstable slopes with satellite Multi Temporal Interferometry: Current issues and future perspectives. *Eng. Geol.* **2014**, *174*, 103–138. [[CrossRef](#)]
37. Sun, H.; Zhang, Q.; Zhao, C.; Yang, C.; Sun, Q.; Chen, W. Monitoring land subsidence in the southern part of the lower Liaohe plain, China with a multi-track PS-InSAR technique. *Remote Sens. Environ.* **2017**, *188*, 73–84. [[CrossRef](#)]

38. Chen, G.; Zhang, Y.; Zeng, R.; Yang, Z.; Chen, X.; Zhao, F.; Meng, X. Detection of land subsidence associated with land creation and rapid urbanization in the Chinese Loess Plateau using time series InSAR: A case study of Lanzhou New District. *Remote Sens.* **2018**, *10*, 270. [[CrossRef](#)]
39. Mario Costantini, T. A novel phase unwrapping method based on network programming. *IEEE Trans. Geosci. Remote Sens.* **1998**, *36*, 813–821. [[CrossRef](#)]
40. Shi, X.; Xu, Q.; Zhang, L.; Zhao, K.; Dong, J.; Jiang, H.; Liao, M. Surface displacements of the Heifangtai terrace in Northwest China measured by X and C-band InSAR observations. *Eng. Geol.* **2019**, *259*, 105181–106193. [[CrossRef](#)]
41. Meldebekova, G.; Yu, C.; Li, Z.; Song, C. Quantifying ground subsidence associated with aquifer overexploitation using space-borne radar interferometry in Kabul, Afghanistan. *Remote Sens.* **2020**, *12*, 2461. [[CrossRef](#)]
42. Jiang, M.; Zhang, F.; Hu, H.; Cui, Y.; Peng, J. Structural characterization of natural loess and remolded loess under triaxial tests. *Eng. Geol.* **2014**, *181*, 249–260. [[CrossRef](#)]
43. Rendell, H.M. Comparison between naturally consolidated and laboratory consolidated loess. *Eng. Geol.* **1988**, *25*, 229–233. [[CrossRef](#)]
44. Jiang, L.; Lin, H. Integrated analysis of SAR interferometric and geological data for investigating long-term reclamation settlement of Chek Lap Kok Airport, Hong Kong. *Eng. Geol.* **2010**, *110*, 77–92. [[CrossRef](#)]
45. Liu, Y.; Li, Y. Environment: China's land creation project stands firm. *Nature* **2014**, *511*, 410. [[CrossRef](#)] [[PubMed](#)]